Inorganic Chemistry

Article

pubs.acs.org/IC

Structural Characterization and Physical Properties of the New Transition Metal Oxyselenide $La_2O_2ZnSe_2$

Andrew J. Tuxworth,[†] Emma E. McCabe,[†] David G. Free,[†] Stewart J. Clark,[‡] and John S. O. Evans*,[†]

[†]Department of Chemistry and [‡]Department of Physics, University Science Site, Durham University, South Road, Durham, DH1 3LE, United Kingdom

S Supporting Information

ABSTRACT: The quaternary transition metal oxyselenide $La_2O_2ZnSe_2$ has been shown to adopt a ZrCuSiAs-related structure with Zn^{2+} cations in a new ordered arrangement within the $[ZnSe_2]^{2-}$ layers. This cation-ordered structure can be derived and described using the symmetry-adapted distortion mode approach. $La_2O_2ZnSe_2$ is an direct gap semiconductor with an experimental optical band gap of 3.4(2) eV, consistent with electronic structure calculations.

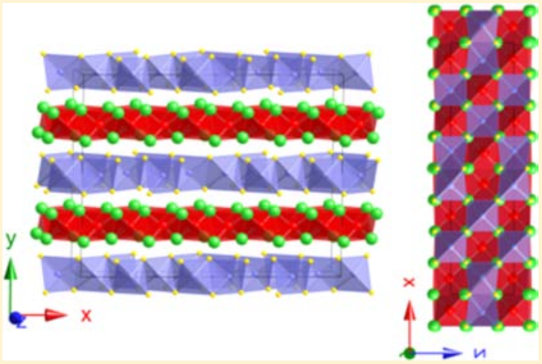

INTRODUCTION

Transition metal oxychalcogenides have a number of interesting physical properties and structural features. LaCuOS, for example, is a wide band gap p-type semiconductor with an optical band gap of 3.1 eV and can be acceptor doped, giving a room-temperature conductivity up to 2.6×10^{-1} S cm^{-1}.[1] It is therefore a promising material for applications in optoelectronic devices. LaCuOS and analogous *Ln*CuO*Q* (*Ln* = La−Nd, Bi; *Q* = S, Se) materials adopt the tetragonal (space group *P*4/*nmm*) ZrCuSiAs structure, illustrated in Figure 1a.[2,3] The structure is built up from alternating layers of fluorite-like $[Ln_2O_2]^{2+}$ sheets and antifluorite-like $[Cu_2Q_2]^{2-}$ sheets. The hole carriers in the p-type semiconductors are thought to be confined to these $[Cu_2Q_2]^{2-}$ sheets,[4] which are composed of edge-linked CuQ_4 tetrahedra. Research on related materials has been motivated by the need for structurally related n-type semiconducting materials as well as materials with different band gaps in order to increase the choice of materials for optoelectronic devices.[5] A related material containing divalent transition metal cations is $La_2O_2CdSe_2$, which has an optical band gap of 3.3 eV but is insulating.[6] With divalent transition metals, the cation sites in the selenide sheets are half occupied, and in $La_2O_2CdSe_2$, this half-occupancy leads to a cation-ordered structure,[4] shown in Figure 1b. Attempts to generate carriers in $La_2O_2CdSe_2$ by introducing Cd or Se vacancies or by aliovalent doping were unsuccessful, and this is attributed to the narrow dispersion of the conduction band, making the conduction band minimum higher than in many other oxychalcogenides.[4]

We report here the synthesis and characterization of the new transition metal oxyselenide $La_2O_2ZnSe_2$. Attempts to synthesize a material of this composition were first reported in 1996 but were unsuccessful, resulting in a mixture of La_2O_2Se and ZnSe.[7] We present work on the structural characterization of $La_2O_2ZnSe_2$ which indicates that the Zn^{2+} cations display a novel ordering pattern within the $[ZnSe_2]^{2-}$ layers. The cation-ordered structure was determined by symmetry-adapted distortion mode analysis of X-ray powder diffraction data, complemented by neutron powder diffraction, single-crystal X-ray diffraction, and electron diffraction. Diffuse reflectance measurements suggest that $La_2O_2ZnSe_2$ is an insulator with an optical band gap of ~3.4(2) eV.

EXPERIMENTAL SECTION

Polycrystalline samples of $La_2O_2ZnSe_2$ were prepared by reaction of La_2O_3 (99.9%, Sigma-Aldrich, heated to 1000 °C prior to use), Se (99.999%, Alfa-Aesar), and Zn (99.9%, Sigma-Aldrich) powders in a 1:2:1 ratio. Reagents were intimately ground and placed in an alumina crucible. Al powder (10% molar excess) was placed in a second alumina crucible to act as an oxygen getter (forming Al_2O_3 during the reaction). These two crucibles were placed in an evacuated silica tube and slowly heated to 1100 °C and held at this reaction temperature for 12 h before furnace cooling to room temperature. The resulting samples were cream colored. Single crystals of $La_2O_2ZnSe_2$ were grown by cooling a polycrystalline sample from 1300 to 800 °C at 0.12 °C min^{-1} in a sealed silica tube under 1×10^{-2} atm of Ar. The resulting crystals were clear, colorless plates of dimensions ≈ 0.08 mm × 0.08 mm × 0.008 mm.

X-ray powder diffraction (XRPD) data were collected using a Bruker D8 diffractometer (operating in reflection mode with Cu $K\alpha_1$ and $K\alpha_2$ radiation, Lynxeye Si strip PSD, step size 0.02°, and variable slits) equipped with an Oxford Cryosystems PheniX cryostat. Samples were sprinkled onto Si zero-background slides covered with a thin

Received: November 14, 2012
Published: January 25, 2013

dx.doi.org/10.1021/ic302484x | *Inorg. Chem.* 2013, 52, 2078−2085

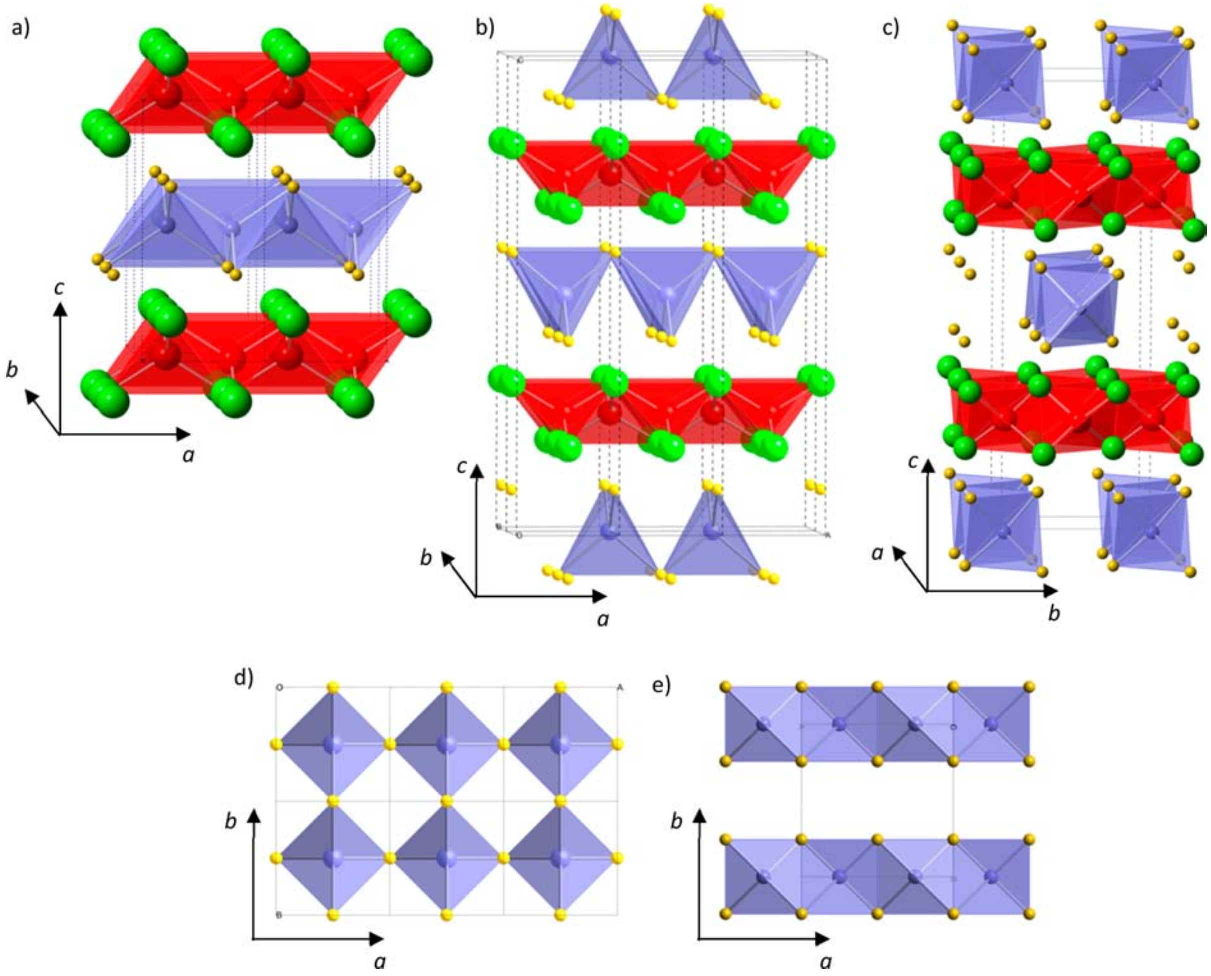

Figure 1. (a) ZrCuSiAs-type structure adopted by LaCuOS showing fluorite-like sheets of edge-linked OLa_4 tetrahedra (red) and antifluorite-like sheets of edge-linked CuS_4 tetrahedra (blue), described by $P4/nmm$ symmetry with $a \approx 4$ Å, $c \approx 9$ Å. (b) Structure of $La_2O_2CdSe_2$ ($P4_2/nmc$ symmetry) with fluorite-like $[La_2O_2]^{2+}$ sheets shown in red and $CdSe_4$ tetrahedra shown in blue. (c) Structure of $Ce_2O_2FeSe_2$ ($Imcb$ symmetry) with fluorite-like $[Ce_2O_2]^{2+}$ sheets in red and $FeSe_4$ tetrahedra in blue. (d) View down [001] in $La_2O_2CdSe_2$ showing the central $[CdSe_2]^{2-}$ sheet with corner-linked $CdSe_4$ tetrahedra. (e) View down [001] in $Ce_2O_2FeSe_2$ showing edge-shared $FeSe_4$ tetrahedra forming stripes; La/Ce^{3+} cations shown in green, and S/Se^{2-} anions shown in yellow.

layer of Vaseline. Room-temperature data were collected for 12 h in the 2θ range 5−120°; 20 min scans were collected at 5 K intervals on cooling and warming between 12 and 300 K. Neutron powder diffraction (NPD) data were collected on the GEM diffractometer (ISIS). A ~2 g sample was loaded into a 6 mm diameter cylindrical vanadium can, and data were acquired for 2 h at room temperature. Powder diffraction data were analyzed by the Rietveld method[8] using the TopasAcademic (TA) software[9,10] controlled using local subroutines. A combined X-ray and neutron (5 detector banks) refinement was carried out using room-temperature scans. The background (shifted Chebyshev), zero point or sample height (DIFA/DIFC for neutron refinements), peak profiles, lattice parameters, atomic positions, isotropic thermal parameters, absorption correction, and a phase fraction of a minor impurity phase of ZnSe (<1%) were refined. A second (<1%) minor unidentified phase is also present. Shorter 20 min XRPD scans collected on cooling and warming were analyzed to determine the temperature dependence of lattice parameters. Single-crystal X-ray diffraction data were collected at 150 K using a Bruker AXS Smart 6000 diffractometer with Mo Kα_1 radiation. Generator settings of 35 kV and 50 mA were used to avoid problems with $\lambda/2$ contamination. Temperature control was achieved using an Oxford Cryosystems Cryostream. A total of 2070 frames were collected in ω steps of 0.3° using a data collection time of 10 s with integration using the SAINT software package.[11] Structure refinements were carried out using the CRYSTALS software package.[12]

Selected area electron diffraction (SAED) data were collected using a Jeol 2100F transmission electron microscope operating at 200 keV. The sample was deposited onto a holey carbon grid. This was mounted in a double-tilt sample holder and zone-axis diffraction patterns were acquired using a Gatan Orius CCD camera. Energy-dispersive X-ray (EDX) data were collected on carbon-coated pellets using a Hitachi SU-70 FEG scanning electron microscope operating at 15 keV, equipped with an Oxford Instruments EDX system.

Diffuse reflectance spectra were obtained by illumination of the sample ground with dry NaCl (~1% w/w) using an Energetiq LDLS EQ-99 broadband lamp and collected at 20° to the excitation using an Ocean Optics Maya Pro 2000 spectrometer. Data were recorded using the Ocean Optics software, and integration times were adjusted to afford maximum response of the spectrometer without saturating the detector. NaCl was used as a reference. Data were used to calculate the reflectance spectra R(I) and then analyzed using the Kubelka−Munk treatment.[13,14]

Electronic structure calculations were performed within the ab initio density functional, plane-wave, pseudopotential formalism as implemented in the Castep[15,16] code. The electronic wave functions are expanded in a plane wave basis set up to a kinetic energy cut off of 340 eV. Electron−ion interactions are described using ab initio, ultrasoft pseudopotentials based on Vanderbilt's formalism.[17] The pseudopotentials treat some of the semicore states as valence, which is important to obtain accurate electronic structures. In particular, this includes the

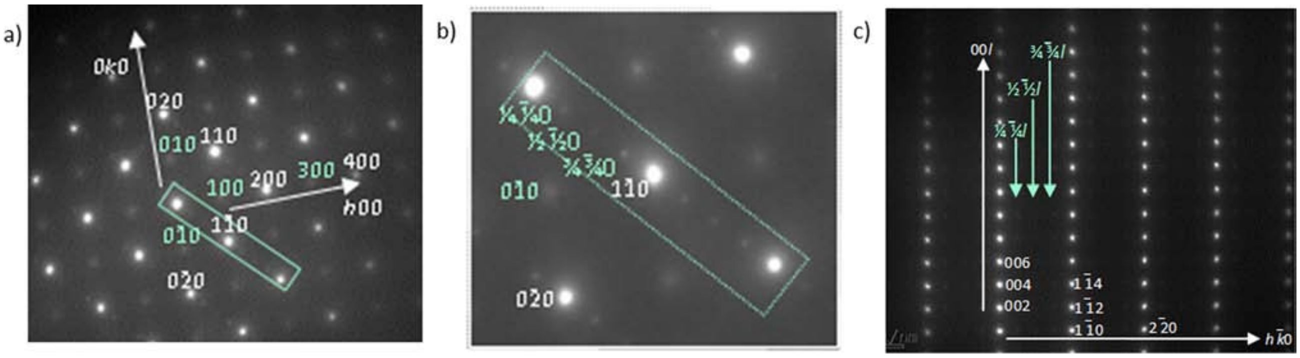

Figure 2. Selected area electron diffraction patterns for $La_2O_2ZnSe_2$ taken down the (a) [001] zone axis and (b) enlarged region showing superstructure reflections and (c) 110 zone axis; zone axes and *hkl* indices of reflections are given relative to the parent *P*4/*nmm* unit cell; those that are consistent with the *P*4/*nmm* structure are shown in white, while those that are inconsistent are shown in green.

full $5s^25p^6$ shells in La and $3d^{10}$ in Zn. Integrations in the Brillouin zone were done with a *k*-point sampling scheme where the *k*-points are spaced at 0.05 $Å^{-1}$. We find that this converges total energy differences to better than 1 meV per atom. Our standard DFT calculations use the PBE[18] exchange-correlation functional; however; we also use the nonlocal screened exchange functional (and norm-conserving pseudopotentials) which has been shown[19] to improve the value of the electronic band gaps in a wide range of materials.

■ RESULTS

Initial Characterization. Preliminary structural characterization of $La_2O_2ZnSe_2$ using lab-based XRPD indicated that it adopts a ZrCuSiAs-related structure with $a \approx 4.05$ Å, $c \approx 8.90$ Å (the subcell), which gives a good fit to the main peaks in the diffraction pattern. However, weak additional reflections were observed at low angles (see section 1 of Supporting Information) which were not accounted for by the tetragonal ZrCuSiAs structure and could not be matched to known impurity phases. The relative intensity of these reflections to the main reflections did not change when attempts were made to prepare off-stoichiometry samples, suggesting that these additional reflections were due to a superstructure of the $La_2O_2ZnSe_2$ phase. Backscattered secondary electron images of $La_2O_2ZnSe_2$ pellets indicate that the sample composition is quite homogeneous. EDX analysis gave the following atomic percentages: La 26(1)%, O 30(1)%, Zn 15.8(4)%, and 27.9(4)%, where the figure in parentheses is the standard deviation of the 30 data points measured, giving an La:O:Zn:Se atomic ratio of 1.9:2.2:1.1:2 consistent with the target composition.

Superstructure Investigation. Attempts to index the weak superstructure reflections observed in XRPD data required a very large unit cell (at least $2\sqrt{2}a_{\text{subcell}} \times \sqrt{2}a_{\text{subcell}} \times 2c_{\text{subcell}}$). Figure 2a shows selected area electron diffraction (SAED) data taken down the [001] zone axis. The strong reflections are consistent with the *P*4/*nmm* parent structure, but weak superstructure reflections are observed along $[1\bar{1}0]$ but not [110] directions. These indicate the loss of tetragonal symmetry in the superstructure. These additional reflections can be indexed as 100, 200, *h*00 ($h = n$) in a $2\sqrt{2}a_{\text{subcell}} \times \sqrt{2}a_{\text{subcell}} \times 2c_{\text{subcell}}$ unit cell or 200, 400, *h*00 ($h = 2n$) in a $4\sqrt{2}_{\text{subcell}} \times \sqrt{2}a_{\text{subcell}} \times 2c_{\text{subcell}}$ unit cell. Figure 2c shows the diffraction pattern taken down the 110 zone axis; weak superstructure reflections (highlighted by green arrows) are again observed, which indicate an increased size of the unit cell in the *ab* plane.

Single-crystal X-ray diffraction data confirmed the need for a supercell of $4\sqrt{2}a_{\text{subcell}} \times \sqrt{2}a_{\text{subcell}} \times 2c_{\text{subcell}}$, although twinning issues (expected for a superstructure of this type) meant that structure solution from single-crystal data was not possible.

Symmetry-Adapted Distortion Mode Analysis. Given the composition of $La_2O_2ZnSe_2$ relative to the LaO*M*Se composition (i.e., $La_2O_2M_2Se_2$) (*M* = monovalent transition metal) of the parent phase, the most likely source of symmetry reduction is ordering of Zn^{2+} cations within the antifluorite-like $[ZnSe_2]^{2-}$ sheets. This lower symmetry structure can be described in terms of the parent structure with symmetry-adapted distortion modes imposed on it. Each mode can distort the parent structure in some way (modes can be displacive, causing a structural distortion, or can act on site occupancies) and may break symmetry elements present in the parent structure, resulting in a reduction in symmetry.[20] Analysis of the possible distortion modes was used to determine the cation ordering pattern in $La_2O_2ZnSe_2$ using the TA Rietveld refinement software.[10] The web-based ISODISTORT software[20] was used to obtain a distortion mode description of the superstructure in *P*1 symmetry including all allowed occupancy and displacive modes. Analysis of the possible occupancy modes (see sections 2−4 of the Supporting Information for the action of important modes) with displacive modes fixed using the "repeated local minimization from random starting values" or RLM method[21] suggested that several occupancy modes (four S2 modes, six S3 modes, two Σ4 modes, and a Γ4− mode) had nonzero amplitudes in the final structures from simulated annealing cycles (see Supporting Information). The process was then repeated but with penalties included on Zn site occupancies to favor models with either fully occupied or fully vacant Zn sites. This reduced the number of modes with nonzero amplitudes to four S2 modes, two S3 modes, a Z2+ mode, and a Γ4− mode (see section 3 of the Supporting Information).

To decide which modes were really important for describing the Zn ordering (i.e., to eliminate potential "phantom modes"[21]), we also performed mode inclusion rounds. The mode inclusion method consists of carrying out cycles of simulated annealing in which each relevant mode is included individually into the fitting process. Its amplitude in the best solution is output, as well as refinement statistics (e.g., R_{wp} or χ^2). It is then removed from the refinement, a different potential mode included, and the process repeated. This method allows the effect of each mode on the fit to the data to be investigated, reducing the problem of correlation between modes. Mode inclusion analysis suggested that two S2 modes at point (1/8 1/8 1/2) (modes 21 and 22) gave a significant improvement in fit (R_{wp} decreased from 10.024% to 7.470%) (Figure 3a). An equally good fit can be obtained by refining either of these modes individually or both simultaneously, suggesting that these modes are correlated. For example, a surface plot showing the fit (measured by R_{wp}) for different amplitudes of the S2 modes at (1/8 1/8 1/2) is shown in section 4 of the Supporting Information. When either of S2 modes 21 or 22 were included in the refinements (forming an "initial mode set"[21]), subsequent rounds of mode inclusion analysis suggested that either of the S2 modes at point (3/8 3/8 1/2) (modes 29 and 30) give a further improvement in fit (decrease in $R_{wp} \approx 0.15\%$) (Figure 3b). When the four S2 modes are included as an initial mode set, a third round of mode inclusion analysis shows that including either of the S3 modes or the Γ4− mode decreases R_{wp} by only 0.06% and 0.03%, respectively (Figure 3c). This improvement in fit from adding S3 (mode 23 or 24) or Γ4− (mode 2) modes was not thought to be significant. These results are consistent with the RLM method with penalties on Zn site occupancies.

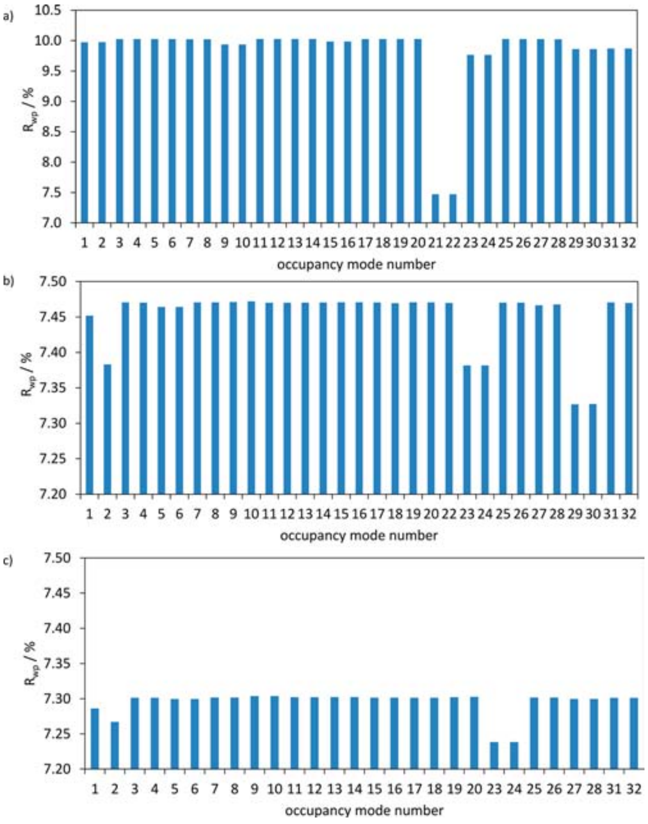

Figure 3. Results from mode inclusion analysis showing (a) initial mode inclusion analysis highlighting improvement in fit on refining amplitudes of S2 modes 21 and 22 at point (1/8 1/8 1/2), (b) second round of mode inclusion analysis showing improvement in fit on addition of either of the S2 modes at point (3/8 3/8 1/2) (mode 29 or 30) to an initial mode set of S2 mode 21, and (c) third round of mode inclusion analysis with four S2 modes (modes 21, 22, 29, and 30) included as initial mode set; minor reductions in R_{wp} are gained by including a Γ4− mode (mode 2) or S3 modes (modes 23 and 24).

With the important modes identified, the RLM method was repeated with just modes 21, 22, 29, and 30 included and penalties on individual Zn site occupancies to favor fully vacant or occupied sites. This indicated that four discrete amplitudes for each of these four modes were observed in the final structures from simulated annealing cycles, giving a total of 16 possible solutions, Figure 4. These different solutions correspond to possible origin choices of the *P*1 unit cell used and give the same cation-ordered structure. We note that this restrained four-mode amplitude model gives an equivalent fit to that obtained with all 32 possible ordering modes refined freely, suggesting these modes are sufficient to describe the symmetry lowering. Using the ISODISTORT software, it is then straightforward to couple the parent structure with these distortion modes and deduce that the material has space group symmetry *Cmca* with basis vectors (4 4 0), (0, 0, −2), (−1, 1, 0) relative to the parent unit cell.

A final combined refinement was carried out using room-temperature XRPD and NPD data with the cation-ordered model of *Cmca* symmetry, illustrated in Figure 5. This gave a good fit to the data and refinement details, selected bond lengths and angles are given in Tables 1−3, and refinement profiles are shown in Figure 6 and in section 6 of the Supporting Information. Bond valence sum calculations[22,23] gave valences of 3.17, 3.02, and 3.11 for La(1), La(2), and La(3), 1.91 and 1.96 for Zn(1) and Zn(2), and 1.74, 1.70, 1.77, 2.38, and 2.27 for Se(1), Se(2), Se(3), O(1), and O(2), respectively. When site occupancies were refined with La occupancy fixed at 1, all other sites refined to within three standard uncertainties of full occupancy, suggesting that the title phase is stoichiometric within the quality of the current data, consistent with the EDX results described above. Although the single-crystal diffraction data are not of high quality, this structural model is consistent with these data.

Structural refinements using XRPD data collected between 12 and 300 K showed smooth increases in unit cell parameters on warming and no evidence for any structural transitions in this temperature range (see Section 7 of Supporting Information). The volume thermal expansion coefficient from 0 to 300 K is $20.5(1) \times 10^{-6}$ K^{-1}.

Diffuse reflectance measurements for $La_2O_2ZnSe_2$ diluted in dry NaCl show a slight decrease in reflectance from low energies followed by a more rapid decrease at wavelengths ≤ 360 nm. The diffuse reflectance spectrum after Kubelka−Munk treatment is shown in Figure 7. Ideally, the intercept of the linear increase in the Kubelka−Munk remission function $F = (1 - R)2/2R$ (R, the diffuse reflectance = I_R/I_0) with the energy axis can be used to determine the optical band gap.[13,14] The spectrum for $La_2O_2ZnSe_2$ shows a slight increase in $F(R)$ with some curvature from low values (∼2 eV), which might indicate the presence of some Se or ZnSe[24] impurities. This is followed by a clear transition with energy 3.4(2) eV, which we assume is due to the optical band gap of $La_2O_2ZnSe_2$.

Electronic structure calculations were carried out using the local functional LDA and the GGA functional PBE and gave almost identical results (see Supporting Information). Both gave an electronic band gap of ∼2 eV and suggest that the valence band maximum (VBM) is predominantly formed from anion p states, while the La^{3+} 5d states are located at the conduction band minimum (CBM). Calculations carried out using the screened potential sX[19] are shown in Figure 8 and indicate that $La_2O_2ZnSe_2$ is a direct band gap semiconductor with a band gap of ∼3.38 eV. These calculations also suggest that the Zn 3d states form a narrow energy band ∼−6 eV, while the VBM is composed of O and Se p states.

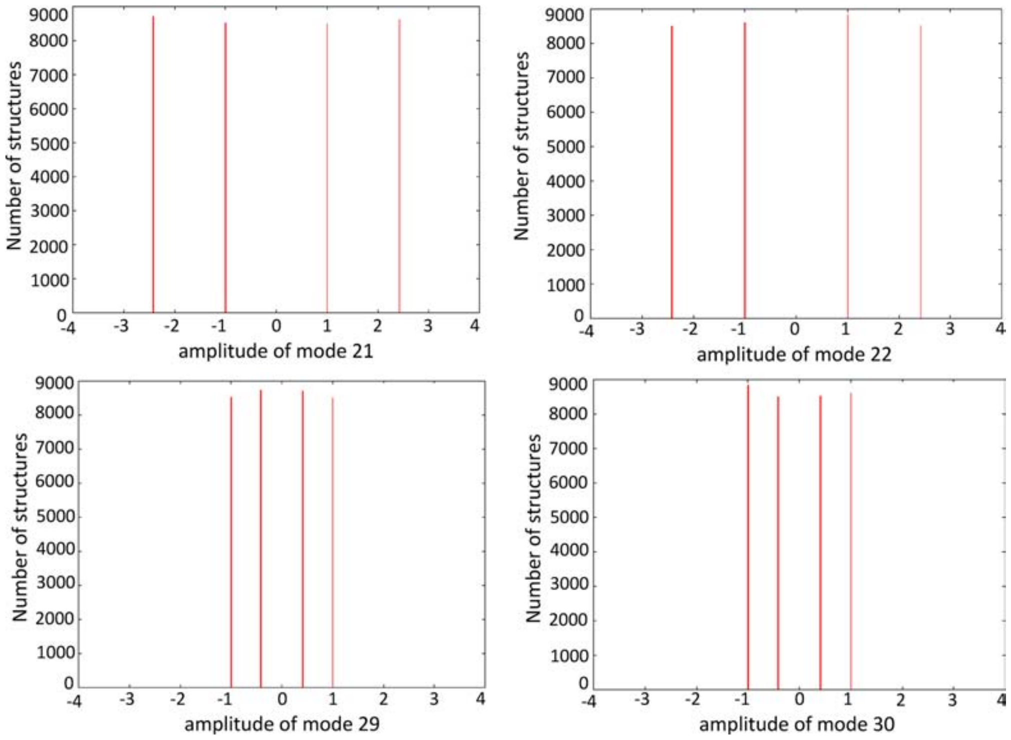

Figure 4. Results from RLM analysis involving only the S2 occupancy modes at (1/8 1/8 1/2) and (3/8 3/8 1/2) with penalties on Zn site occupancies to favor fully occupied or vacant sites showing multiconvergence histograms for these four S2 modes; these results indicate amplitudes of ±1.00, ± 2.414 for S2 modes at (1/8 1/8 1/2) (modes 21 and 22) and amplitudes of ±1.00, ± 0.414 for S2 modes at (3/8 3/8 1/2) (modes 29 and 30).

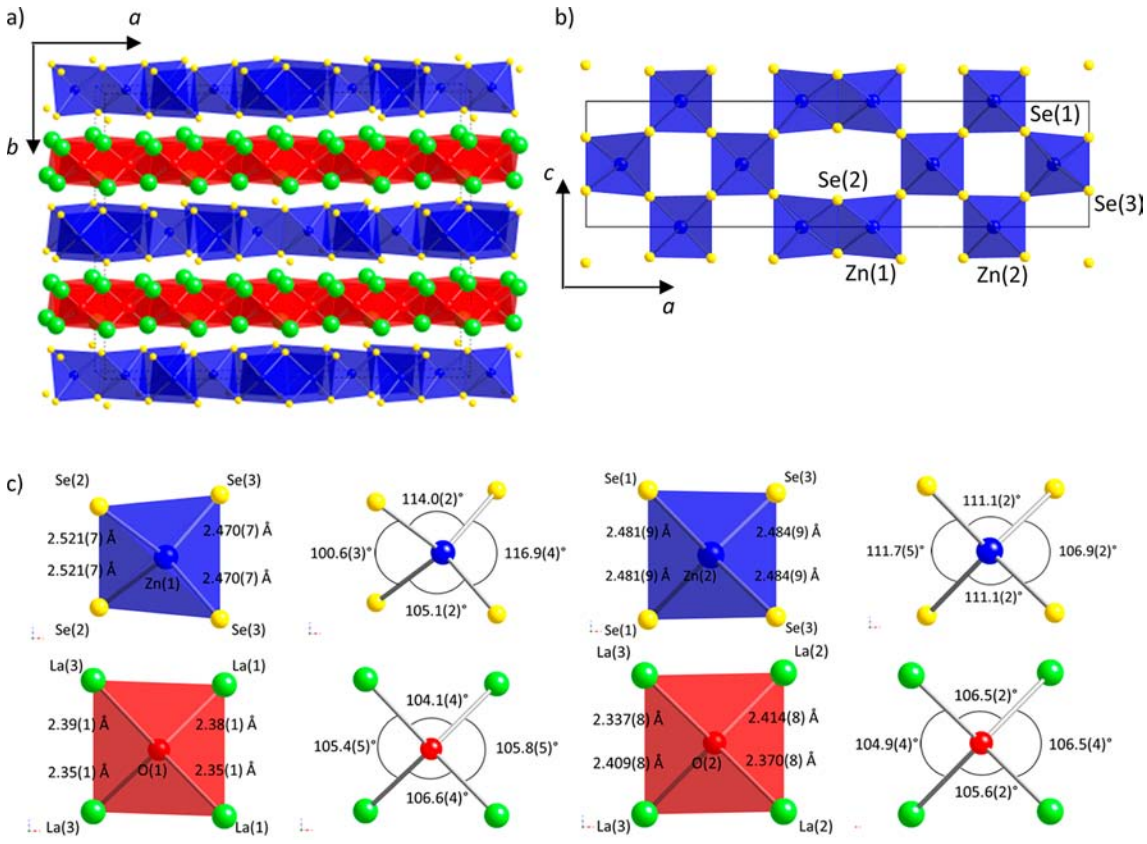

Figure 5. Crystal structure of $La_2O_2ZnSe_2$ showing (a) alternating $[La_2O_2]^{2+}$ and $[ZnSe_2]^{2-}$ layers in red and blue, respectively, (b) ordering pattern of Zn^{2+} cations in $[ZnSe_2]^{2-}$ layers, and (c) coordination polyhedra for Zn and O sites; La, Zn, O, and Se ions are shown in green, blue, red, and yellow, respectively.

Table 1. Structural Parameters of $La_2O_2ZnSe_2$ from Combined Refinement Using Room-Temperature XRPD and NPD Data in Space Group *Cmca*[a]

atom	Wyckoff site	*x*	*y*	*z*	occupancy	$B/Å^2$
La(1)	8e	0.25	0.1811(3)	0.25	1	0.27(9)
La(2)	8f	0	−0.1785(3)	−0.2229(6)	1	0.16(7)
La(3)	16g	−0.3745(2)	0.3185(2)	0.2674(5)	1	0.27(6)
Zn(1)	8d	−0.4298(2)	0	0	1	0.9(1)
Zn(2)	8d	−0.1893(5)	0	0	1	0.40(8)
Se(1)	8e	0.25	0.4174(7)	0.25	1	0.6(1)
Se(2)	8f	0	−0.4148(4)	−0.2109(9)	1	0.7(1)
Se(3)	16g	−0.3735(3)	0.0835(4)	0.2600(6)	1	0.45(7)
O(1)	16g	−0.3121(5)	0.2469(2)	0.503(2)	1	0.66(8)
O(2)	16g	0.4376(4)	0.2487(4)	0.5243(9)	1	0.26(6)

[a] $a = 22.9332(2)$ Å, $b = 17.80043(6)$ Å, $c = 5.73241(6)$ Å; $R_{wp} = 5.233\%$, $R_p = 4.433\%$, and $\chi^2 = 6.538$.

Table 2. Selected Bond Lengths for $La_2O_2ZnSe_2$ from Combined Refinement Using Room-Temperature XRPD and NPD Data in Space Group *Cmca*

La(1)−O(1)	2 × 2.35(1) Å 2 × 2.38(1) Å	Zn(1)−Se(2)	2 × 2.521(7) Å
La(2)−O(2)	2 × 2.370(8) Å 2 × 2.414(8) Å	Zn(1)−Se(3)	2 × 2.470(7) Å
La(3)−O(1)	1 × 2.35(1) Å 1 × 2.39(1) Å	Zn(2)−Se(1)	2 × 2.481(9) Å
La(3)−O(2)	1 × 2.337(8) Å 1 × 2.409(8) Å	Zn(2)−Se(3)	2 × 2.484(9) Å

■ DISCUSSION

The structure of $La_2O_2ZnSe_2$ is closely related to that of the LaCuOS family of materials and contains La_4O tetrahedra which edge share to form sheets perpendicular to the *b* axis of the material. These lanthanum oxide sheets alternate with sheets containing $ZnSe_4$ tetrahedra. The divalent nature of the transition metal means only one-half the tetrahedral sites are occupied relative to LaOCuS materials. Three other divalent transition metal systems have been described: $La_2O_2CdSe_2$ discussed above, Figure 1b; $CeOMn_{0.5}Se$, with the tetrahedral sites in the antifluorite-like $[Mn_{0.5}Se]^-$ sheets half-occupied in a disordered manner;[25] and $Ce_2O_2FeSe_2$ with Fe^{2+} cations ordered into stripes of edge-shared $FeSe_4$ tetrahedra,[26] Figure 1c.

The ordering pattern of Zn^{2+} cations in $La_2O_2ZnSe_2$ contains a mixture of edge- and corner-sharing tetrahedra, resulting in alternating "checkerboard" and "stripe" regions along the [100] direction, Figure 5b. It is thus intermediate between the $Ce_2O_2FeSe_2$ and the $La_2O_2CdSe_2$ structures.[27] Distortion mode refinement (using both displacive and occupancy degrees of freedom) suggests that site ordering is the main driver for the symmetry lowering. The most significant structural distortions (see section 5 of the Supporting Information) are two Γ1+ modes which act on the La(2) and Se(2) sites and displace them in the *z* direction (but do not lead to further symmetry lowering). The effect of Γ1+ on Se(2) is to give rise to the distortion of Zn(1)Se4 edge-shared tetrahedra, shown in Figure 5b. As expected, the Zn−Zn separation in these edge-shared tetrahedra is significantly longer than in an idealized structure (3.22 vs ∼2.875 Å). The observed Γ1+ distortion effectively reduces the Zn(1)−Se(2) distance from ∼2.66 to ∼2.52 Å, reducing underbonding at Zn(1). Displacement of La(2) sites is smaller and presumably optimizes the bonding around Se(2). From a purely geometric viewpoint, the Zn ordering pattern is surprising as the checkerboard arrangement of $La_2O_2CdSe_2$ would be expected as it minimizes electrostatic repulsions compared to the stripe arrangement of $Ce_2O_2FeSe_2$. Observation of stripes in the more covalent Fe system is consistent with this argument. The differing arrangement between Zn and Cd materials could also arise due to strain effects arising from the size mismatch between ideal layers of OLa_4 edge-sharing tetrahedra and differing arrangements of MSe_4 tetrahedra. Detailed discussion of this is beyond the scope of the current paper.

While the model proposed here gives an excellent fit to X-ray and neutron diffraction data, there are a few weak reflections observed in SAED patterns that are not consistent with this *Cmca* model and which we do not believe are due to kinematical effects. These reflections, indexed as 401, 403, 12 0 1, *h*0*l*... ($h = 4n$, $l \neq 2n$) in the *Cmca* unit cell, would be permitted in the subgroup $C222_1$ (where S3 modes 23 and 24 and Γ4− mode 2, Figure 3c, would also be potentially active). Refinements in $C222_1$ gave only a marginal reduction in R_{wp} (5.298% to 5.242% for equivalent combined refinements) despite a significant increase in the number of structural variables (28 to 50) and a structure essentially unchanged from the *Cmca* model. We therefore prefer the *Cmca* model given the data available.

The large optical band gap measured here for $La_2O_2ZnSe_2$ (3.4(2) eV) is comparable to that reported for $La_2O_2CdSe_2$ (3.3 eV),[4,6] consistent with the similar colors of these two

Table 3. Selected Bond Angles for $La_2O_2ZnSe_2$ from Combined Refinement Using Room-Temperature XRPD and NPD Data in Space Group *Cmca*

La(1)−O(1)−La(1)	105.8(5)°	Se(2)−Zn(1)−Se(2)	100.6(3)°
La(1)−O(1)−La(3)	104.1(4), 106.6(4)°	Se(3)−Zn(1)−Se(3)	116.9(4)°
La(2)−O(2)−La(2)	106.5(4)°	Se(2)−Zn(1)−Se(3)	105.1(2)°, 114.0(2)°
La(2)−O(2)−La(3)	105.6(2), 106.5(2)°	Se(1)−Zn(2)−Se(1)	111.7(5)°
La(3)−O(1)−La(3)	105.4(5)°	Se(3)−Zn(2)−Se(1)	111.1(2)°
La(3)−O(2)−La(3)	104.9(4)°	Se(3)−Zn(2)−Se(3)	109.2(5)°, 106.9(3)°

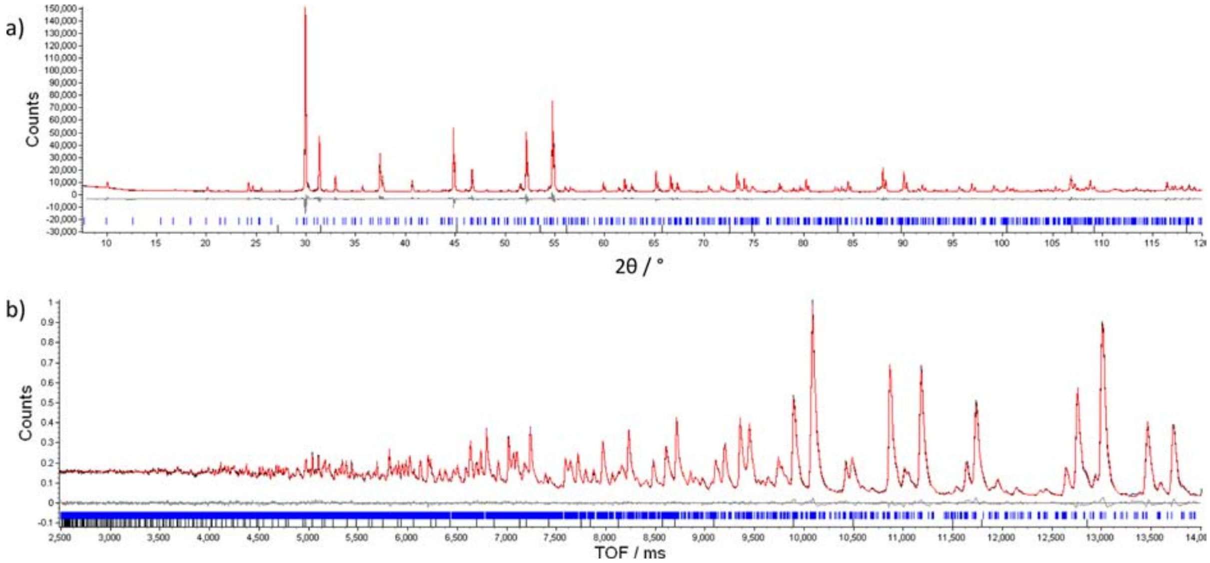

Figure 6. Rietveld refinement profiles from combined refinement using room-temperature (a) XRPD and (b) NPD data for $La_2O_2ZnSe_2$, refined in space group *Cmca* (observed, calculated, and difference profiles shown in black, red, and gray, respectively); tick marks show reflection positions for $La_2O_2ZnSe_2$ (top) and ZnSe (bottom, <1% by weight).

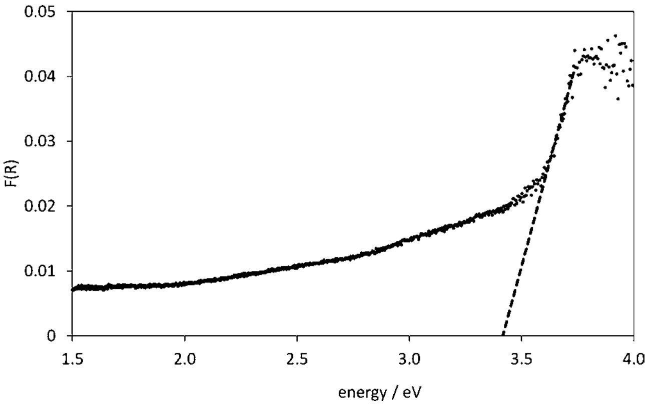

Figure 7. Diffuse reflectance spectrum after Kubelka−Munk treatment for $La_2O_2ZnSe_2$ diluted in dry NaCl, showing interband transition corresponding to an optical band gap of 3.4(2) eV.

quaternary oxyselenides ($La_2O_2ZnSe_2$ is a cream color; $La_2O_2CdSe_2$ is pale yellow). This band gap is noticeably larger than that observed for binary ZnSe (~2.67 eV).[28,29] As discussed for the analogous cadmium materials,[4] this increase in band gap is likely to be the result of decreased bandwidth/band narrowing due to the layered structure of the quaternary oxyselenides.[30] We note that the sX screened potential gives good agreement with the experimental band gap, whereas in both the Zn (Section 8 of Supporting Information) and Cd systems,[4] the GGA and PBE functionals significantly underestimate it. We expect the observed optical band gap to be close in energy to the electronic band gap for a direct band gap material such as this. The electronic structures calculated for ZnSe and $La_2O_2ZnSe_2$ share some similar features including upper valence bands (−5 − 0 eV) composed mainly of Se 4p-derived states and fairly localized Zn 3d states at ~−6 eV. However, O 2p states also contribute to the upper valence band in $La_2O_2ZnSe_2$, extending it to lower energies. The band derived from Zn 3d states is slightly narrower in $La_2O_2ZnSe_2$ compared with ZnSe, perhaps reflecting the reduced Zn content compared with the 1:1 binary selenide.

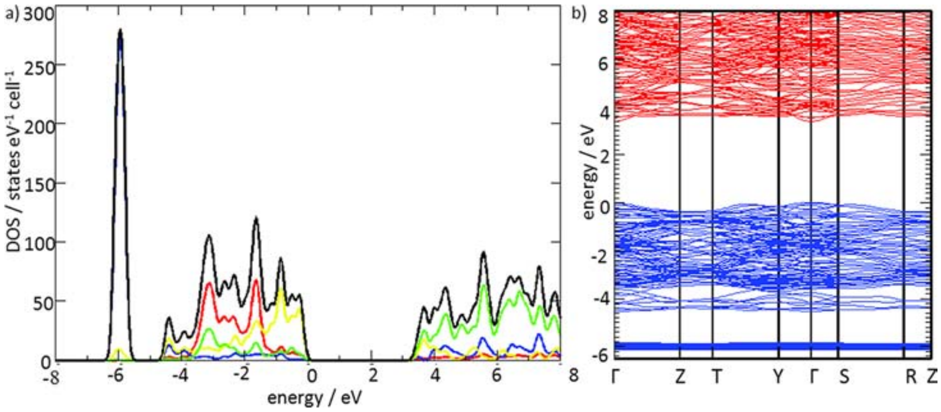

Figure 8. (a) Projected densities of states with contributions from Zn, La, O, and Se in blue, green, red, and yellow, respectively, and total density of states in black, and (b) calculated band structure for $La_2O_2ZnSe_2$, where the upper valence states are shown in blue and lower conduction states in red; the top of the valence band is taken as zero on the energy axis.

■ CONCLUSION

We describe here the synthesis, structural characterization, and optical measurements of the new material $La_2O_2ZnSe_2$. It adopts a ZrCuSiAs-related structure with ordering of Zn^{2+} cations over the tetrahedral sites in the $[ZnSe_2]^{2-}$ layers that can be deduced a priori using symmetry-adapted distortion modes. The ordering pattern is unusual in that it contains both stripe-like and checkerboard-like features and is intermediate between ordering patterns observed for $La_2O_2CdSe_2$ and $Ce_2O_2FeSe_2$. Diffuse reflectance measurements indicate that $La_2O_2ZnSe_2$ is a wide band gap semiconductor with an optical band gap of 3.4(2) eV, which is consistent with electronic structure calculations using the screened potential sX.

■ ASSOCIATED CONTENT

Ⓢ Supporting Information

Rietveld refinement profiles for refinement of ZrCuSiAs structural model for $La_2O_2ZnSe_2$; table of occupancy mode number, label, *k*-point and order parameter direction; results from RLM analysis showing multiconvergence histograms for each of the occupancy mode amplitudes of *P*1 symmetry for a $4\sqrt{2}a \times \sqrt{2}a \times 2c$ model of $La_2O_2ZnSe_2$; description and schematic representation of Zn-ordered structures; surface plot showing the fit (measured by R_{wp}) to XRPD data for different amplitudes of modes 21 and 22; results from mode inclusion analysis on displacive modes; Rietveld refinement profiles; lattice parameters for $La_2O_2ZnSe_2$ as a function of temperature; projected densities of states for $La_2O_2ZnSe_2$; a cif file of the final refinement. This material is available free of charge via the Internet at http://pubs.acs.org.

■ AUTHOR INFORMATION

Corresponding Author

*E-mail: john.evans@durham.ac.uk.

Notes

The authors declare no competing financial interest.

■ ACKNOWLEDGMENTS

We are grateful to Dr. Ron Smith and the GEM Express scheme at ISIS for NPD data and to Professor Andy Beeby for help with diffuse reflectance measurements. We thank EPSRC and Durham University for funding. We are grateful to Dr. Branton Campbell and Dr. Simon Willerton for helpful discussions. We thank UKCP and EPSRC for use of the UK supercomputer (Hector) under grant EP/F037481/1.

■ REFERENCES

(1) Ueda, K.; Inoue, S.; Hirose, S.; Kawazoe, H.; Hosono, H. *Appl. Phys. Lett.* **2000**, *77* (17), 2701−2703.

(2) Hiramatsu, H.; Yanagi, H.; Kamiya, T.; Ueda, K.; Hirano, M.; Hosono, H. *Chem. Mater.* **2008**, *20*, 326−334.

(3) Ueda, K.; Takafuji, K.; Hiramatsu, H.; Ohta, H.; Kamiya, T.; Hirano, M.; Hosono, H. *Chem. Mater.* **2003**, *15*, 3692−3695.

(4) Hiramatsu, H.; Ueda, K.; Kamiya, T.; Ohta, H.; Hirano, M.; Hosono, H. *J. Mater. Chem.* **2004**, *14*, 2946−2950.

(5) Hiramatsu, H.; Kamioka, H.; Ueda, K.; Ohta, H.; Kamiya, T.; Hirano, M.; Hosono, H. *Phys. Status Solidi A* **2006**, *203* (11), 2800−2811.

(6) Hiramatsu, H.; Ueda, K.; Kamiya, T.; Ohta, H.; Hirano, M.; Hosono, H. *J. Phys. Chem. B* **2004**, *108*, 17344−17351.

(7) Baranov, I. Y.; Dolgikh, V. A.; Popovkin, B. A. *Russ. J. Inorg. Chem.* **1996**, *41* (11), 1916−1919.

(8) Rietveld, H. M. *J. Appl. Crystallogr.* **1969**, *2*, 65.

(9) Coelho, A. A. *J. Appl. Crystallogr.* **2003**, *36*, 86.

(10) Coelho, A. A. *TOPAS Academic: General Profile and Structure Analysis Software for Powder Diffraction Data*, 5th ed.; Bruker AXS: Karlsruhe, Germany, 2012.

(11) *SAINT*, Bruker AXS: Madison, WI, 2005.

(12) Betteridge, P. W.; Carruthers, J. R.; Cooper, R. I.; Prout, K.; Watkin, D. J. *J. Appl. Crystallogr.* **2003**, *36*, 1487.

(13) Kortum, G.; Braun, W.; Herzog, G. *Angew. Chem., Int. Ed.* **1963**, *2* (7), 333−404.

(14) Tandon, S. P.; Gupta, J. P. *Phys. Status Solidi* **1970**, *38*, 363−366.

(15) Segall, M. D.; Lindan, P. J. D.; Probert, M. J.; Pickard, C. J.; Hasnip, P. J.; Clark, S. J.; Payne, M. C. *J. Phys.: Condens. Matter* **2002**, *14* (11), 2717−2744.

(16) Clark, S. J.; Segall, M. D.; Pickard, C. J.; Hasnip, P. J.; Probert, M. J.; Refson, K.; Payne, M. C. *Z. Kristallogr.* **2005**, *220* (5−6), 567−570.

(17) Vanderbilt, D. *Phys. Rev. B* **1990**, *41*, 7892−7895.

(18) Perdew, J. P.; Burke, K.; Ernzerhof, M. *Phys. Rev. Lett.* **1996**, *77*, 3865−3868.

(19) Clark, S. J.; Robertson, J. *Phys. Rev. B* **2010**, *82* (8), 085208.

(20) Campbell, B. J.; Stokes, H. T.; Tanner, D. E.; Hatch, D. M. *J. Appl. Crystallogr.* **2006**, *39*, 607−614.

(21) Kerman, S.; Campbell, B. J.; Satyavarapu, K. K.; Stokes, H. T.; Perselli, F.; Evans, J. S. O. *Acta Crystallogr.* **2012**, *A68*, 222−234.

(22) Brese, N. E.; O'Keefe, M. *Acta Crystallogr.* **1991**, *B47*, 192−197.

(23) Brown, I. D.; Altermatt, D. *Acta Crystallogr.* **1985**, *B41*, 244−247.

(24) Peng, Q.; Dong, Y.; Li, Y. *Angew. Chem., Int. Ed.* **2003**, *42*, 3027−3030.

(25) Ijjaali, I.; Mitchell, K.; Haynes, C. L.; McFarland, A. D.; Duyne, R. P. V.; Ibers, J. A. *J. Solid State Chem.* **2003**, *176*, 170−174.

(26) McCabe, E. E.; Free, D. G.; Evans, J. S. O. *Chem. Commun.* **2011**, *47*, 1261−1263.

(27) It is noted that $Ce_2O_2FeSe_2$ adopts a ZrCuSiAs-related structure, while the lanthanum analogue β-$La_2O_2FeSe_2$ adopts a different structure with quite different Fe−Se layers.

(28) Adachi, S.; Taguchi, T. *Phys. Rev. B* **1991**, *42* (12), 9569−9577.

(29) Aven, M.; Marple, D. T. F.; Segall, B. *J. Appl. Phys.* **1961**, *32* (10), 2261−2265.

(30) Zhu, J.-X.; Yu, R.; Wang, H.; Zhao, L. L.; Jones, M. D.; Dai, J.; Abrahams, E.; Morosan, E.; Fang, M.; Si, Q. *Phys. Rev. Lett.* **2009**, *104*, 216405.